Three-nucleon forces and spectroscopy of neutron-rich calcium isotopes

J. D. Holt,[1,2,3,*] J. Menéndez,[1,2,†] J. Simonis,[1,2,‡] and A. Schwenk[1,2,§]

[1]*Institut für Kernphysik, Technische Universität Darmstadt, 64289 Darmstadt, Germany*

[2]*ExtreMe Matter Institute EMMI, GSI Helmholtzzentrum für Schwerionenforschung GmbH, 64291 Darmstadt, Germany*

[3]*National Superconducting Cyclotron Laboratory and Department of Physics and Astronomy, Michigan State University, East Lansing, Michigan 48844, USA*

(Received 30 May 2014; published 18 August 2014)

We study excited-state properties of neutron-rich calcium isotopes based on chiral two- and three-nucleon interactions. We first discuss the details of our many-body framework, investigate convergence properties, and for two-nucleon interactions benchmark against coupled-cluster calculations. We then focus on the spectroscopy of $^{47-56}$Ca, finding that with both 3N forces and an extended $pfg_{9/2}$ valence space, we obtain a good level of agreement with experiment. We also study electromagnetic transitions and find that experimental data are well described by our calculations. In addition, we provide predictions for unexplored properties of neutron-rich calcium isotopes.

DOI: 10.1103/PhysRevC.90.024312 PACS number(s): 21.10.−k, 21.30.−x, 21.60.Cs, 27.40.+z

I. INTRODUCTION

Understanding the evolution of shell structure from the valley of stability to neutron-rich extremes represents a key challenge in nuclear structure [1,2]. With a closed proton shell, the calcium isotopes provide an ideal region to investigate shell formation and evolution in medium-mass nuclei from nuclear forces. The rich shell structure beyond ^{48}Ca, combined with the capabilities of rare-isotope beam facilities, has lead to an intensive focus on calcium isotopes, where new measurements provide exciting tests and constraints for state-of-the-art many-body methods and nuclear forces.

Recent experiments have established new shell closures in exotic calcium isotopes. A possible $N = 32$ closure in ^{52}Ca was first recognized from a higher first-excited 2^+ (2^+_1) energy [3,4], more than 1.5 MeV higher than the 2^+_1 energy in the neighboring ^{50}Ca. Moreover, signatures of a $N = 32$ magic number were discovered in nearby titanium and chromium isotopes [5–8]. These observations have been complemented by high-precision mass measurements, which revealed a flat behavior of the two-neutron separation energy S_{2n}, leading up to the shell closure at ^{52}Ca [9]. Groundbreaking mass measurements out to ^{54}Ca [10] discovered a steep decrease in S_{2n} from ^{52}Ca to ^{54}Ca. Combined with the high two-neutron shell gap $S_{2n}(Z,N) - S_{2n}(Z,N+2)$, this unambiguously established $N = 32$ as a prominent shell closure [10]. Evidence for a $N = 34$ shell closure has proven more elusive, as the 2^+_1 energy is not high in the neighboring titanium or chromium isotopes [11–14]. Very recently, the 2^+_1 energy in ^{54}Ca was found to be only ∼500 keV below that in ^{52}Ca [15], suggesting a new shell closure. Mass measurements through ^{56}Ca will be essential to establish the closed-shell nature of ^{54}Ca. In addition, the spectroscopy of neutron-rich calcium isotopes provides valuable information, with important tests of theoretical calculations [16–18].

Previous work for the calcium isotopes includes phenomenological valence-space [19–23] or beyond-mean-field calculations [24]. While these approaches are generally successful in reproducing experiment up to ^{52}Ca, disagreement is significant in ^{53,54}Ca, which led to many experimental and theoretical efforts aiming to clarify the nature of $N = 34$ in calcium. The uncertainty in extrapolating phenomenological models to exotic nuclei shows the importance of developing systematic many-body approaches based on nuclear forces. Such calculations were initially pursued based on two-nucleon (NN) forces but failed to reproduce the standard $N = 28$ shell closure and other key features in calcium for $A \gtrsim 47$ [19,25]. Neglected three-nucleon (3N) forces were suggested to be the crucial missing ingredient [26].

The calcium region currently represents a frontier for *ab initio* calculations based on NN and 3N forces [27]. The first application of 3N forces in calcium was in the context of valence-space Hamiltonians [28], which demonstrated the important role of 3N forces in reproducing the dripline and spectra in oxygen isotopes [29,30], as well as in proton-rich nuclei [31]. In calcium isotopes, 3N forces provided the first microscopic explanation for the $N = 28$ magic number in ^{48}Ca, as well as for the ground-state energies [28]. The improved calculations of Refs. [9,10,32] successfully predicted the additional binding found in ^{52}Ca [9] as well as the behavior of the two-neutron separation energy from $^{48-54}$Ca [10]. Coupled-cluster (CC) calculations, including continuum degrees of freedom and phenomenological 3N forces, also found a very good description of these signatures [33]. This agreement extends to *ab initio* self-consistent Green's function (SCGF) calculations with chiral NN and 3N forces [34,35]. In addition, the CC calculations of Ref. [36] and the *ab initio* in-medium similarity renormalization group (IMSRG) [37,38] have been applied to the calcium isotopes.

In this paper, we present a comprehensive study of excited-state properties of neutron-rich calcium isotopes based on our valence-space approach of Refs. [9,10,28–32], focusing in

*Present address: TRIUMF, 4004 Wesbrook Mall, Vancouver, BC, V6T 2A3, Canada; jholt@triumf.ca

†javier.menendez@physik.tu-darmstadt.de

‡simonis@theorie.ikp.physik.tu-darmstadt.de

§schwenk@physik.tu-darmstadt.de

particular on shell structure in the region around $N = 28,32,34$. In Sec. II, we discuss details of the calculation of valence-space Hamiltonians perturbatively based on NN and 3N forces from chiral effective field theory (EFT) [39,40]. We investigate convergence both order by order in many-body perturbation theory and in terms of intermediate-state excitations, with NN interactions evolved to low momentum via renormalization-group (RG) methods. For NN interactions, we benchmark against CC calculations and find reasonable agreement. In Sec. III, we calculate spectra and electromagnetic transitions in $^{47-56}$Ca, showing that, with 3N forces and an extended valence space, good agreement with experiment is obtained, in many cases comparable to phenomenological interactions. Finally, we explore the role of residual 3N forces. Similar to the oxygen isotopes [41], their impact on spectra is minor, while for ground-state energies their contributions increase with the number of valence nucleons.

II. MICROSCOPIC VALENCE-SPACE HAMILTONIANS

A. Many-body perturbation theory

For a given nucleus, the solution of the A-body Schrödinger equation with the Hamiltonian H gives the eigenstates $|\psi_n\rangle$ and energies E_n,

$$H|\psi_n\rangle = (H_0 + V)|\psi_n\rangle = E_n|\psi_n\rangle, \tag{1}$$

where H_0 defines a single-particle basis $|\phi_n\rangle$ with corresponding eigenvalues ϵ_n,

$$H_0|\phi_n\rangle = \epsilon_n|\phi_n\rangle, \tag{2}$$

and V includes the interactions between nucleons. Solving the A-body Schrödinger equation in a large single-particle basis by diagonalization is challenging due to the large number of configurations involved. Therefore, many-body methods generally take one of two strategies to describe medium-mass nuclei. In approaches such as CC theory [33,36,42], SCGF theory [34,35], or the IMSRG [37,38], all nucleons are active, but some truncations are necessary in practice. In valence-space methods, the number of degrees of freedom is reduced by treating the nucleus as a many-body system comprised of a closed-shell core, with the additional nucleons occupying a truncated single-particle (valence) space. After deriving an effective valence-space Hamiltonian, this is then diagonalized exactly in the valence space.

We first define operators P and Q, which project into and out of the valence space, respectively:

$$P = \sum_{i=1}^{d} |\phi_i\rangle\langle\phi_i|, \tag{3}$$

$$Q = 1 - P, \tag{4}$$

where d is the dimension of the valence space, $P^2 = P$, $Q^2 = Q$, and $PQ = 0$. Then, the goal is to construct an effective valence-space Hamiltonian $H_{\rm eff}$,

$$PH_{\rm eff}P|\psi_\alpha\rangle = E_\alpha P|\psi_\alpha\rangle, \tag{5}$$

with

$$H_{\rm eff} = \sum_{i=1}^{d} \varepsilon_i a^\dagger a + V_{\rm eff}, \tag{6}$$

which after diagonalization in the valence space reproduces a subset E_α of eigenvalues of the full A-body Hamiltonian. Here, ε_i are the single-particle energies (SPEs) of the d orbitals in the valence space and $V_{\rm eff}$ is the effective interaction between valence nucleons.

Many-body perturbation theory (MBPT) provides a diagrammatic framework to calculate both the SPEs ε_i and $V_{\rm eff}$ from nuclear forces [25,43–45]. This approach has been pursued with NN interactions but, due to poor agreement with experiment, all shell-model calculations in practice involve adjustments of either the SPEs, $V_{\rm eff}$, or both. To calculate $H_{\rm eff}$ we start from an energy-dependent effective interaction between valence nucleons, the $\widehat{Q}$ box, which takes into account excitations outside the valence space,

$$\widehat{Q}(\omega) = PVP + PVQ\frac{1}{\omega - QHQ}QVP, \tag{7}$$

and is evaluated at the unperturbed starting energy $\omega = PH_0P$. The diagrammatic expansion of $\widehat{Q}$ consists of all irreducible, valence-linked diagrams. To remove the energy dependence, we include folded diagrams through a nonperturbative transformation involving $\widehat{Q}$ and its energy derivatives. This results in an energy-independent, size-extensive effective interaction

$$V_{\rm eff}^{(k)} = \widehat{Q} + \sum_{m=1}^{\infty} \frac{1}{m!}\left(\frac{d^m\widehat{Q}}{d\omega^m}\right)\left(V_{\rm eff}^{(k-1)}\right)^m. \tag{8}$$

This integral equation is solved by iteration, which converges when $V_{\rm eff}^{(k)} \approx V_{\rm eff}^{(k-1)}$, typically after $\sim$15 iterations. We make two approximations in our evaluation of $\widehat{Q}$. First we truncate $\widehat{Q}$ at some finite order. In this work we include contributions up to third order in MBPT, the current state of the art. Second, excitations out of the valence space are allowed to some finite energy $N\hbar\omega$, which is ultimately limited by the size of the single-particle basis. Convergence with respect to these two approximations is discussed in Sec. II C.

We then calculate the SPEs in ^{41}Ca consistently from the corresponding set of one-body diagrams, the $\widehat{S}$ box, also taken to third order in MBPT in the same harmonic-oscillator basis as the $\widehat{Q}$ box. To obtain the single-particle energies, we solve the coupled Dyson equations,

$$\varepsilon_i^{(k)} = \langle i|H_0|i\rangle + \widehat{S}_i\left(\varepsilon_i^{(k-1)}\right), \tag{9}$$

by iteration starting from $\varepsilon_i^{(0)} = \omega$ until $\varepsilon_i^{(k)} \approx \varepsilon_i^{(k-1)}$. Because the ε_i depend on relative shifts in the unperturbed harmonic-oscillator spectrum, we also update the unperturbed valence-space energy to be the centroid of the converged SPEs and iterate until the centroid of the final SPEs is equal to the unperturbed value. Convergence is reached after $\sim$10 iterations.

B. Nuclear interactions

Our results are based on nuclear forces derived in chiral EFT, a systematic expansion for nuclear forces [39,40] in

which 3N interactions arise naturally at next-to-next-to-leading order (N^2LO). At the NN level, we perform a RG evolution [46,47] of the 500 MeV N^3LO NN potential of Ref. [48] by using a smooth regulator [49] with $\Lambda = 2.0\,\mathrm{fm}^{-1}$, to obtain a low momentum interaction, $V_{\mathrm{low}\,k}$. The RG evolution decouples low from high momenta and improves the convergence of the MBPT calculation [47]. At the 3N level, we use the leading N^2LO 3N forces [50,51], which include a long-range two-pion-exchange part, a shorter-range one-pion exchange, and a 3N contact interaction. The two undetermined 3N couplings are fit to the ^{3}H binding energy and the ^{4}He radius at the same resolution scale as the $V_{\mathrm{low}\,k}$ interaction [52].

In the calculation of valence-space Hamiltonians, we include normal-ordered one- and two-body parts of 3N forces, which correspond to interactions among one valence and two core nucleons, or two valence and one core nucleon, respectively. These give rise to repulsive interactions among valence neutrons and increase the spin-orbit splitting in the SPEs [28,29]. They are expected to be dominant over residual 3N forces between three valence particles because of phase-space considerations [53]. This has been confirmed in CC calculations of light and medium-mass nuclei [36,54]. In Sec. III D, we explore this by calculating the contributions from residual 3N forces [10,41] for ground and first-excited states.

We work in a harmonic-oscillator basis with $\hbar\omega = 11.48$ MeV and include NN forces in 13 major shells and 3N forces in 5 major shells. When 3N forces are included fully to third order in MBPT, we find that the contribution to SPEs range from ∼1 to 6 MeV for different orbitals, approximately an order of magnitude larger than the effects on valence-space interactions, as expected from the hierarchy of normal-ordered contributions [54]. Moreover, with 3N forces, the calculated SPEs are comparable to the empirical values of the phenomenological GXPF1A [22] and KB3G [20] interactions for the pf-shell orbitals [28,32], as shown in Table I.

TABLE I. Phenomenological and calculated (MBPT) SPEs in MeV. Details are given in the text.

Orbital	Phenomenological		MBPT
	GXPF1A [22]	KB3G [20]	$pfg_{9/2}$
$f_{7/2}$	−8.62	−8.60	−8.05
$p_{3/2}$	−5.68	−6.60	−5.86
$p_{1/2}$	−4.14	−4.60	−3.22
$f_{5/2}$	−1.38	−2.10	−1.33
$g_{9/2}$	(−1.00)		−1.23

C. Convergence properties

Next, we discuss the convergence properties of MBPT when using low-momentum NN interactions. For a fixed valence space, the results must converge order by order in the $\hat{Q}$- and $\hat{S}$-box expansion as well as in the allowed intermediate-state excitations. Because the RG evolution renders nuclear interactions more perturbative and decouples low- from high-oscillator states, improved convergence behavior is expected in both respects [47].

Assessing order-by-order convergence beyond third order is a challenge for MBPT, since complete fourth-order calculations are beyond current computational capabilities and have not been attempted. In Fig. 1, we show the order-by-order convergence of the ground-state energies of ^{42,48}Ca as a function of increasing intermediate-state excitations $N\hbar\omega$, within a harmonic-oscillator basis of 13 major shells. $N\hbar\omega$ denotes the number of excitation quanta in a given intermediate-state configuration (e.g., two neutrons excited three shells above the valence space is a $6\hbar\omega$ excitation). In these studies, we use NN-only forces with empirical SPEs and see promising order-by-order behavior: the change from second to third order is ∼15% of the change from first to second order. While the calculations cannot be said to be completely converged at third order, this trend suggests that changes due to a complete fourth-order calculation would be small. In particular, they will be less important than other uncertainties in the calculation, such as the uncertainties in the input Hamiltonian.

We also observe in Fig. 1 that in terms of intermediate-state excitations, the convergence with $V_{\mathrm{low}\,k}$ is rapid, with third

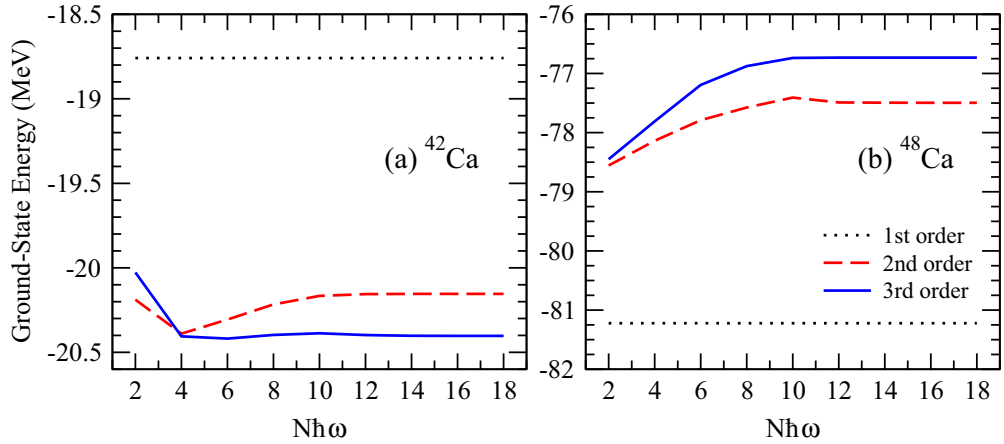

FIG. 1. (Color online) Convergence of the (a) ^{42}Ca and (b) ^{48}Ca ground-state energies as a function of increasing intermediate-state excitations $N\hbar\omega$ and perturbative order. Calculations are based on NN forces in 13 major harmonic-oscillator shells.

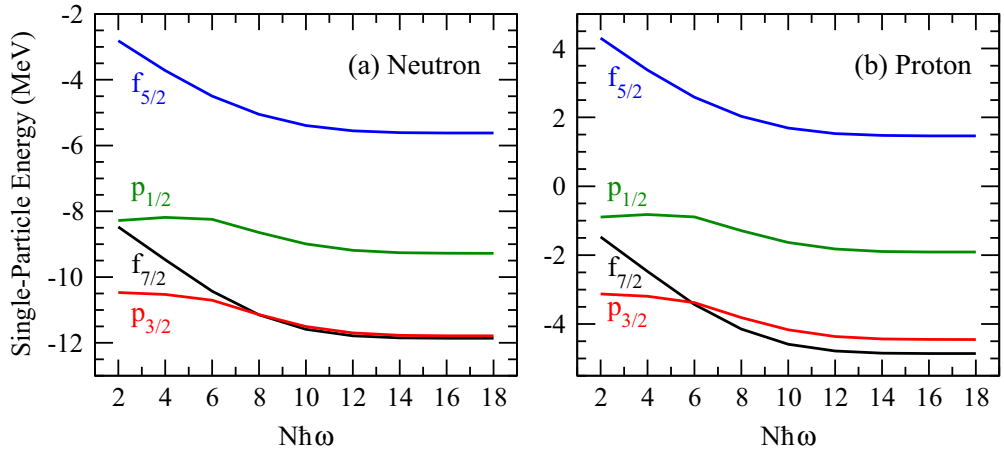

FIG. 2. (Color online) Convergence of (a) neutron and (b) proton SPEs as a function of increasing intermediate-state excitation $N\hbar\omega$. Calculations are based on NN forces in 13 major harmonic-oscillator shells.

order converging faster than second order. For all orders, the ground-state energies of both ^{42,48}Ca are well converged by $\sim 12\hbar\omega$. Similarly, Fig. 2 shows the convergence of neutron and proton SPEs in the pf-shell as a function of $N\hbar\omega$. While convergence is slower compared to the ground-state energies, all SPEs are converged by $14\hbar\omega$, with neutron and proton SPEs following a very similar convergence pattern. Finally, all calculations with 3N forces seem to be converged when included in five major shells. In two-body matrix elements and SPEs, the change from four to five major shells is $\sim$10 keV and $\sim$50 keV, respectively. Work to extend 3N forces beyond five major shells is currently in progress.

D. Benchmark with coupled-cluster theory

We can also benchmark the MBPT energies with *ab initio* methods by using identical starting interactions and working in the same single-particle basis. Here, we perform CC calculations for the ground-state energies of the calcium isotopes by using the same $V_{\mathrm{low}\,k}$ interaction in a single-particle basis of 13 major harmonic-oscillator shells with $\hbar\omega = 12$ MeV. The results are shown in Fig. 3 relative to the ground-state energy of ^{40}Ca. The closed j-subshell systems ^{40,48,52,54,60}Ca are calculated at the Λ-CCSD(T) level [42,55]. The $A \pm 1$ systems ^{47,49,51,53,55,59}Ca are obtained with the CC particle-attached-or-removed equations of motion method at the singles and doubles level (PA-PR-EOM-CCSD) [42,55].

To compare with CC results, we perform the MBPT calculations in the pf shell, where the SPEs are taken as the PA-EOM-CCSD ($f_{7/2}$, $p_{3/2}$, $p_{1/2}$, $f_{5/2}$) energies in ^{41}Ca. The particle-attached $g_{9/2}$ is not of single-particle character, so the MBPT pf-shell comparison provides the cleanest benchmark. This comparison probes the two-body part of the valence-space Hamiltonian, assessing the reliability of the convergence trend illustrated in Fig. 1.

In Fig. 3, we find that the MBPT ground-state energies are within 5% (in most cases much better) of those of CC theory. This shows that MBPT can be comparable to CC theory for $V_{\mathrm{low}\,k}$ interactions, provided that consistent SPEs are employed.

While the CC ground-state energies agree well with MBPT to ^{55}Ca, this agreement deteriorates for heavier isotopes. The reason is that the CC calculations begin to fill the $g_{9/2}$ orbit, which is lower in energy than the calculated $f_{5/2}$. This makes a comparison of the CC and pf-shell valence-space calculations unreliable for ^{59,60}Ca. Moreover, a benchmark in the $pfg_{9/2}$ space is not possible because, as mentioned, the CC one-particle-attached $g_{9/2}$ state in ^{41}Ca is not of single-particle character.

E. Valence-space calculations

For neutron-rich oxygen and calcium isotopes, we have shown that it is necessary in MBPT calculations of valence-space Hamiltonians to expand the valence space beyond the standard one-major harmonic-oscillator shell [28,30–32].

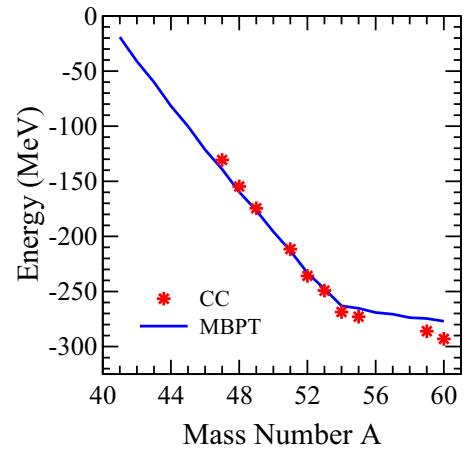

FIG. 3. (Color online) Comparison of MBPT and CC ground-state energies of calcium isotopes relative to ^{40}Ca based on the same NN interaction (for details see text). The MBPT results use the SPEs obtained in CC theory.

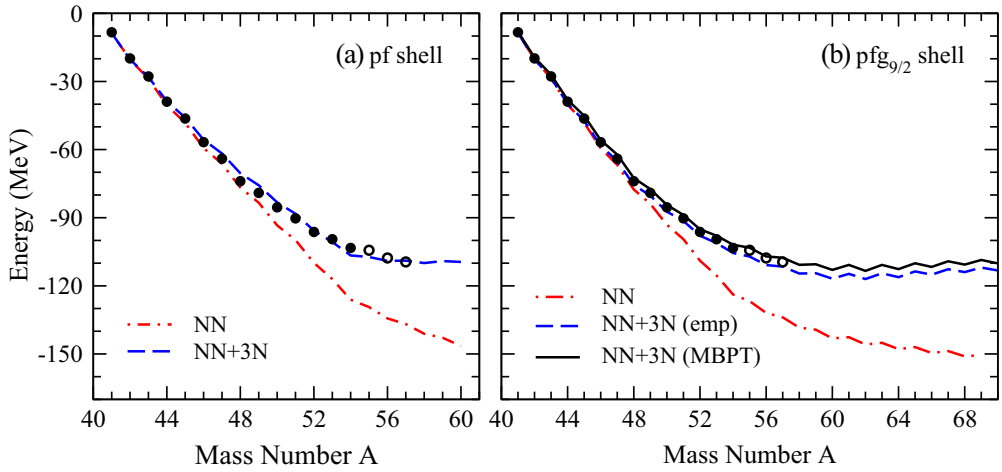

FIG. 4. (Color online) Calculated ground-state energies of calcium isotopes in (a) pf shell and (b) $pfg_{9/2}$ shell compared with experimental data (solid points) and AME2012 extrapolated values (open circles) [59]. Calculations are performed in the extended $pfg_{9/2}$ valence space and based on NN forces only, NN + 3N forces with empirical SPEs, and NN + 3N forces with calculated (MBPT) SPEs.

This takes into account the effects of the additional orbitals nonperturbatively, so that the general strategy is to make the valence space for diagonalization as large as possible and include the contributions beyond the valence space in MBPT, which converges better for larger valence spaces.

In this work, we perform calculations in both the $0f_{7/2}$, $1p_{3/2}$, $0f_{5/2}$, $1p_{1/2}$ valence space (pf shell) and the extended space including the $0g_{9/2}$ orbit ($pfg_{9/2}$ valence space), in both cases on top of a ^{40}Ca core. We take two approaches with respect to SPEs: in all pf-shell calculations we use the empirical GXPF1A SPEs, while for the $pfg_{9/2}$ space we either use the GXPF1A values (setting $g_{9/2} = -1.0$ MeV), or the MBPT SPEs calculated consistently, as shown in Table I. The shell model codes ANTOINE [19,56] and NATHAN [19] have been used throughout this work.

The $pfg_{9/2}$ space consists of orbitals beyond one-major harmonic-oscillator shell, which means that the center-of-mass (c.m.) motion of the valence nucleons will not factorize in general. Following Refs. [57,58], we have investigated possible c.m. contamination in our calculations by adding a c.m. Hamiltonian, $\beta H_{\text{c.m.}}$, with $\beta = 0.5$, to our original Hamiltonian. This has a modest impact on excitation spectra, where states can be affected up to ∼200 keV. This difference can be understood because the nonzero c.m. two-body matrix elements are also relevant matrix elements of the MBPT calculation, and a clear separation between these two effects is difficult. Similarly, we find non-negligible $\langle H_{\text{c.m.}} \rangle$ values, which point to possible c.m. admixture and/or non-negligible occupancies of the $g_{9/2}$ orbital.

There are several directions in progress to investigate this further in both the $pfg_{9/2}$ and $sdf_{7/2}p_{3/2}$ [30] spaces. We will carry out a nonperturbative Okubo–Lee–Suzuki–Okamoto transformation [60,61] into the standard one-major-shell space, which is free of c.m. spurious states. This will keep the treatment of the orbitals within the extended space nonperturbative, while treating the MBPT configurations perturbatively. We will also apply the IMSRG [37] to extended valence spaces, tailoring the evolution so that the cross-shell matrix elements have small values: $\langle H_{\text{c.m.}} \rangle \to 0$. Finally, we will explore different valence spaces, choosing the core of the calculations so that the c.m. factorizes. For instance, for the neutron-rich calcium isotopes a ^{48}Ca core can be used. Here, we follow the calculations of ground-state energies of Refs. [9,10,32] and present results for the spectra for the same interactions.

III. RESULTS

A. Ground-state energies

The calculated ground-state energies for calcium isotopes are shown for both the pf and $pfg_{9/2}$ shells in Fig. 4. These are the same as for the predictions of the neutron-rich $^{51-54}$Ca reported in Refs. [9,10]. They update the results of Ref. [28], where 3N forces where included only to first order in MBPT. The repulsive effect of normal-ordered 3N forces [28,29] is evident in both valence spaces, and there is only a small difference between the calculations with empirical and calculated (MBPT) SPEs, which reflects the similar values shown in Table I.

While the pf and $pfg_{9/2}$ spaces give similar absolute ground-state energies, detailed comparisons to recent experimental two-neutron separation energies [9,10] and three-point mass differences [9,32] highlight the good agreement found with the $pfg_{9/2}$-shell results. Beyond ^{60}Ca, the ground-state energies evolve very flatly with A, which makes a precise prediction of the dripline difficult. Moreover, for masses beyond ^{54}Ca, CC calculations indicate that continuum degrees of freedom play an important role in lowering the $1d_{5/2}$ and $2s_{1/2}$ orbitals, which are not included in our calculations. As a result these orbitals may become degenerate with $0g_{9/2}$ near ^{60}Ca, and further lowering of the ground-state energies beyond ^{60}Ca is expected [33]. Therefore, to explore reliably the neutron-rich region towards the dripline, continuum degrees of freedom and larger valence spaces are necessary.

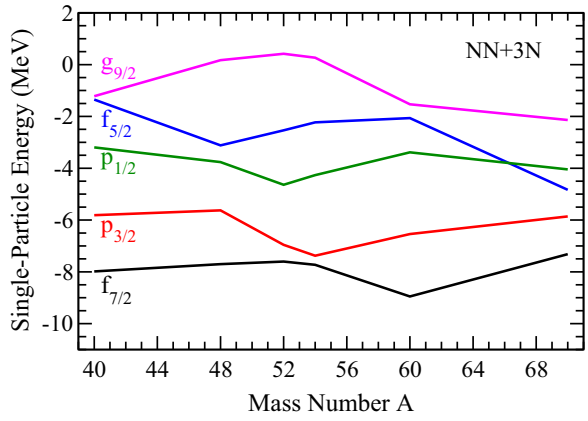

FIG. 5. (Color online) Evolution of SPEs as a function of mass number. Calculations are based on NN + 3N forces in the extended $pfg_{9/2}$ space.

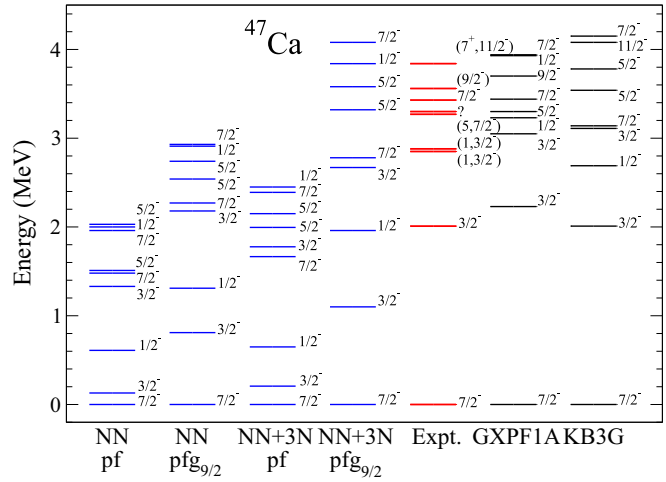

FIG. 6. (Color online) Excitation energies of bound excited states in ^{47}Ca compared with experiment [62] and phenomenological GXPF1A [22] and KB3G [20] interactions. The NN-only results are calculated in the pf and $pfg_{9/2}$ spaces with empirical SPEs. The NN + 3N results are obtained in the same spaces. In the pf shell, empirical SPEs are used, while the $pfg_{9/2}$-space results use the consistently calculated MBPT SPEs.

B. Spectra

We now calculate the spectra of neutron-rich calcium isotopes, comparing our MBPT predictions to experiment when available, as well as to shell-model results by using the phenomenological interactions GXPF1A [22] and KB3G [20]. We discuss in detail the spectra of the neutron-rich isotopes $^{47–56}$Ca. For $^{47–50}$Ca we present different calculations based on chiral interactions and compare to experiment, emphasizing the importance of extended valence spaces and 3N forces. To quantify these effects in excitation spectra, we show results with NN forces only and NN + 3N forces, in the pf-shell and in the extended $pfg_{9/2}$ space. For $^{51–56}$Ca, where there is no or limited experimental information on excited states, we focus on the predictions of our best calculations (NN + 3N forces in the $pfg_{9/2}$ space). The spectra for the lighter $^{42–46}$Ca, which mostly probe the $f_{7/2}$ orbital, are given in Appendix.

To understand these results, we refer to the effective single-particle energies (ESPEs), given in Fig. 5, for NN + 3N forces in the $pfg_{9/2}$ space, which describe the evolution of the spherical mean field of the calculation. While correlations are important in the final results and are included via exact diagonalization, ESPEs provide a guide to the position of different orbitals for a given neutron number within our valence-space framework. The important role of the extended valence spaces is manifested in the occupancies of the $g_{9/2}$ orbital. For ground states, these become significant in ^{47}Ca, with the $g_{9/2}$ occupation number 1.2 increasing to 2.1 in ^{56}Ca. They are accompanied by a depletion of the $f_{7/2}$ occupations.

1. ^{47}Ca

In Fig. 6 we show the calculated spectra for ^{47}Ca in the pf and $pfg_{9/2}$ spaces using NN-only and NN + 3N forces. In the pf-shell calculations, the spectra are too compressed. The two lowest-lying states differ by only 200 keV, and there is otherwise very poor agreement with experiment. Furthermore, the effects of 3N forces in the pf shell are relatively small. Extending the calculation to the $pfg_{9/2}$ space with NN forces only partially improves the spectrum, but it remains too compressed. Our final results with NN + 3N forces in the extended space improve the spectrum, leading to the best agreement with experiment.

Nevertheless, we still observe deficiencies in our MBPT spectrum. The major disagreement is in the lowest $3/2^-$ state, which is approximately 1 MeV below experiment, reflecting the small $f_{7/2}$-$p_{3/2}$ gap around ^{48}Ca, as seen in Fig. 5. This state is well reproduced by the phenomenological interactions. Similarly, the $1/2^-_1$ state is also low, due to the small $f_{7/2}$-$p_{1/2}$ gap in our calculations.

2. ^{48}Ca

Figure 7 shows the calculated ^{48}Ca spectra compared with experiment. As with ^{47}Ca we note that the pf space generally gives overly compressed spectra, and 3N forces give only minor improvements. In the extended $pfg_{9/2}$ space, while NN forces also give a poor experimental description, significant improvement is obtained when 3N forces are included.

The gap between the ground state and the 2^+_1 state, a measure of the shell closure at $N = 28$, is well reproduced, although somewhat overpredicted by 500 keV. As we have a relatively small $f_{7/2}$-$p_{3/2}$ gap in the ESPEs in Fig. 5, the high 2^+_1 state is a result of correlations involving $g_{9/2}$, in particular $f_{7/2}$-$g_{9/2}$. On the other hand, we find a 0^+ as the first-excited state, contrary to experiment, in all calculations. Since this state is dominated by the $2p$-$2h$ configuration with respect to the ground state of the form $(f_{7/2})^{-2}(p_{3/2})^2$, this may be related to an overly strong $f_{7/2}$-$p_{3/2}$ pairing interaction. Other excited states are in good agreement with experiment and are comparable to the results of GXPF1A and KB3G.

3. ^{49}Ca

As in lighter isotopes, our calculations of ^{49}Ca in Fig. 8 show that, with either NN forces only or in the pf shell, the

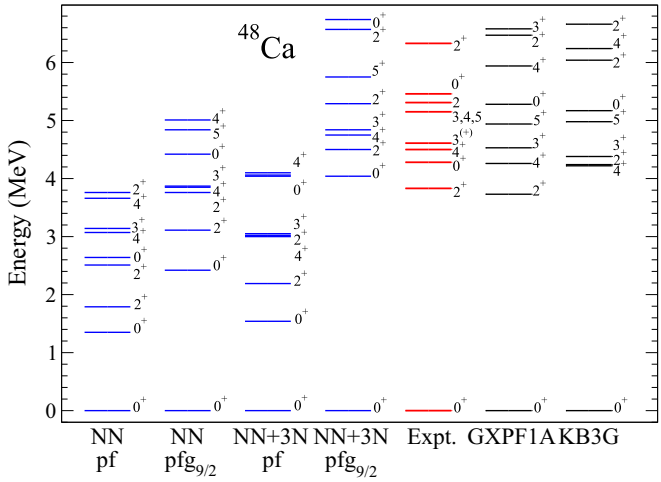

FIG. 7. (Color online) Excitation energies of bound excited states in ^{48}Ca compared with experiment [62] and phenomenological interactions (labels are as in Fig. 6).

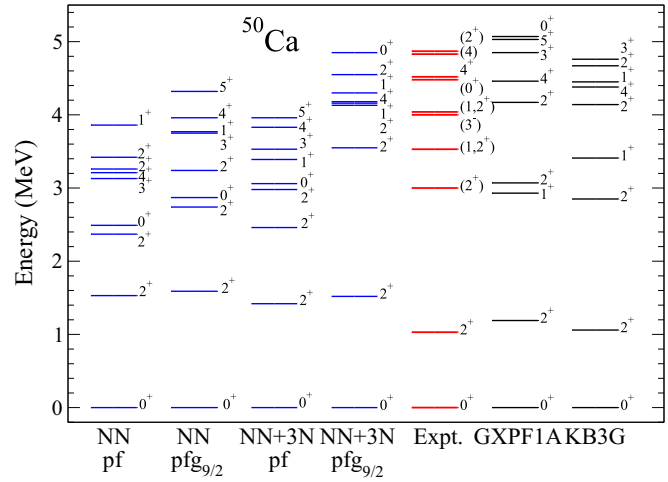

FIG. 9. (Color online) Excitation energies of bound excited states in ^{50}Ca compared with experiment [18,62] and phenomenological interactions (labels are as in Fig. 6).

physics necessary to reproduce the spectrum is not adequately captured; the excited states are too compressed and with incorrect ordering. It is only in the NN + 3N calculations in the extended $pfg_{9/2}$ space that we observe a reasonable description of the ^{49}Ca spectrum.

The ground state in ^{49}Ca is dominated by the single-particle configuration of a $p_{3/2}$ particle on top of ^{48}Ca. Therefore, the first excited $1/2^-_1$ state, predicted in very good agreement with experiment, reflects the effective $p_{3/2}$-$p_{1/2}$ gap for this nucleus. Also the location of the lowest $7/2^-_1$ state is in reasonable agreement with the tentatively assigned experimental level (it lies some 500 keV lower), and with predictions from the phenomenological interactions. This state is dominated by a $2p$-$1h(f_{7/2})^{-1}(p_{3/2})^2$ configuration on top of ^{48}Ca and therefore reflects the effective $f_{7/2}$-$p_{3/2}$ gap plus correlations discussed for the closure of ^{48}Ca.

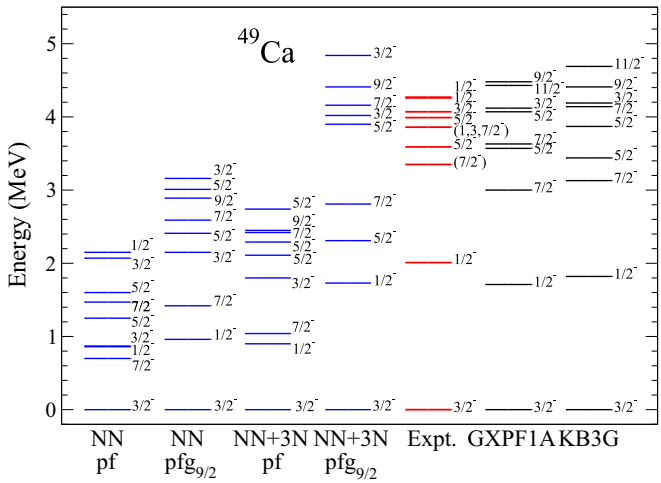

FIG. 8. (Color online) Excitation energies of bound excited states in ^{49}Ca compared with experiment [18,62] and phenomenological interactions (labels are as in Fig. 6).

However, in our calculations we observe that the $5/2^-_1$ state is quite low compared with experiment and the phenomenological interactions. This is indicative of a small effective $p_{3/2}$-$f_{5/2}$ gap in this region. We also note that the spin of the fourth excited state has not been experimentally identified, but that our calculations, as in phenomenology, predict it as a $7/2^-$ state.

4. ^{50}Ca

In Fig. 9 we see that, for ^{50}Ca, the location of the first excited 2^+_1 state is overpredicted in all MBPT calculations by ~500 keV. The 0^+ ground state and the 2^+_1 state are dominated by $(p_{3/2})^2$ configurations. Therefore, the increased 2^+_1 energy is related to the low excited 0^+ state found in ^{48}Ca.

Although most of the experimental spin and parity assignments are tentative, in our calculations with NN + 3N forces in the $pfg_{9/2}$ space, the remaining states are compatible with experiment and comparable to the results with the phenomenological interactions. In particular, the large 2 MeV gap between the 2^+_1 and 2^+_2 states is not reproduced in our other MBPT calculations. The location of the lowest 1^+_1 state differs significantly in the three calculations, which are otherwise consistent with the data, with the MBPT prediction being 1 MeV and 500 keV above the GXPF1A and KB3G predictions, respectively. A reliable assignment of the spin of the third excited state in ^{50}Ca at 3.53 MeV is needed to identify this state and test the theoretical calculations.

5. ^{51}Ca

In ^{51}Ca there is no definite experimental information on the spins of the excited states, only tentative assignments based largely on inferences from phenomenological interactions [14,17]. Therefore, we show in Fig. 10 only our NN + 3N calculation in the extended $pfg_{9/2}$ space and compare with

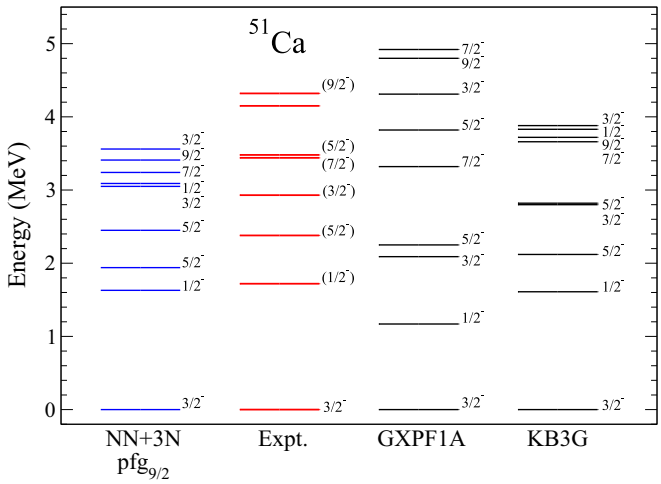

FIG. 10. (Color online) Excitation energies of bound excited states in ^{51}Ca compared with experiment [14,17] and phenomenological interactions (labels are as in Fig. 6).

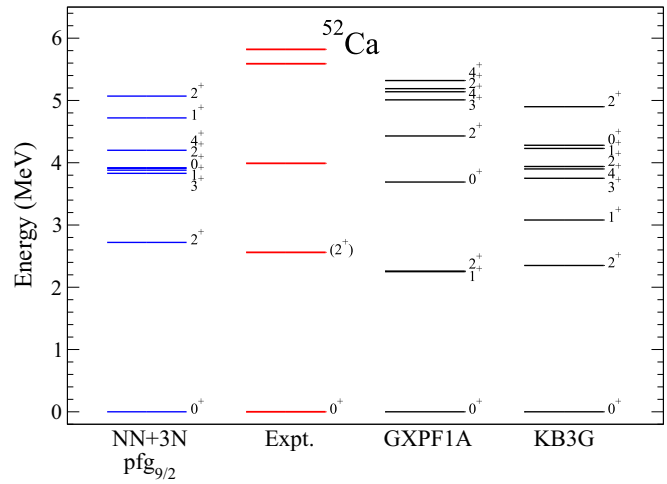

FIG. 11. (Color online) Excitation energies of bound excited states in ^{52}Ca compared with experiment [14,17] and phenomenological interactions (labels are as in Fig. 6).

the experimental excitation energies and with the phenomenological results.

The $3/2^-$ ground state is dominated by a $p_{3/2}$ hole configuration below the $N = 32$ subshell closure. The first excited $1/2^-$ state is indicative of the effective $p_{3/2}$-$p_{1/2}$ gap (and approximate strength of the $N = 32$ closure) and is in very good agreement with the experimental tentative spin assignment and the results of the phenomenological interactions. The $5/2^-$ state with dominant $1p$-$1h(p_{3/2})^{-1}(f_{5/2})^1$ configuration above the ground state is the $5/2^-_1$ state in our calculation, while in the phenomenological interactions it is the $5/2^-_2$ state, lying 1 MeV higher for KB3G and 2 MeV higher for GXPF1A. The reason for the difference when using 3N forces is related to the low $5/2^-$ state in ^{49}Ca, originating from the small effective $p_{1/2}$-$f_{5/2}$ gap in our MBPT approach. Note that this effective gap is also significantly different between the phenomenological interactions. In turn, the $5/2^-_2$ state in the MBPT calculations has a $(p_{3/2})^2_{J=2}(p_{1/2})^1$ dominant structure (on top of ^{48}Ca) and is therefore related to the 2^+_1 state in ^{50}Ca. In all calculations it agrees with the tentatively assigned experimental state at 2.4 MeV. Ultimately, improved γ-ray spectroscopy is needed.

6. ^{52}Ca

For ^{52}Ca, there are no spin assignments except for the ground and first-excited state, where the large spacing was first identified as a signature of the $N = 32$ subshell closure [3]. The strong $N = 32$ shell closure has been unambiguously established with mass measurements out to ^{54}Ca, leading to a steep decrease of the two-neutron separation energy after ^{52}Ca [10]. In Fig. 11 our NN + 3N calculations are compared to the phenomenological interactions. All agree well with the limited experimental data.

One striking difference between models, however, is the location of the 1^+_1 state, which is found in our MBPT calculations 1 and 2 MeV above the KB3G and GXPF1A calculations, respectively, and hence an accurate experimental measurement would be highly valuable. The 3^+_1 state is also predicted quite differently depending on the calculation; our MBPT value is in good agreement with KB3G but more than 1 MeV below that of GXPF1A.

7. ^{53}Ca

Only the ground-state spin of ^{53}Ca and the position of two excited states are known experimentally; one of them only measured very recently at Rikagaku Kenkyusho (RIKEN, the Institute of Physical and Chemical Research of Japan) [15]. Figure 12 shows our NN + 3N calculations in the $pfg_{9/2}$ space compared to the phenomenological interactions. In this spectrum the ground state is dominated by a $p_{1/2}$ hole in the $N = 34$ closed subshell. Therefore, the difference between the ground and first $5/2^-_1$ and $3/2^-_1$ states will be related to the effective $p_{1/2}$-$f_{5/2}$ and $p_{1/2}$-$p_{3/2}$ gaps and hence the

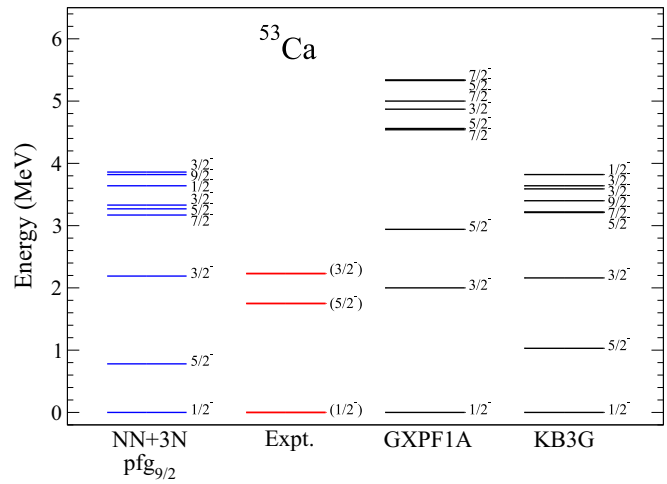

FIG. 12. (Color online) Excitation energies of bound excited states in ^{53}Ca compared with experiment [15] and phenomenological interactions (labels are as in Fig. 6).

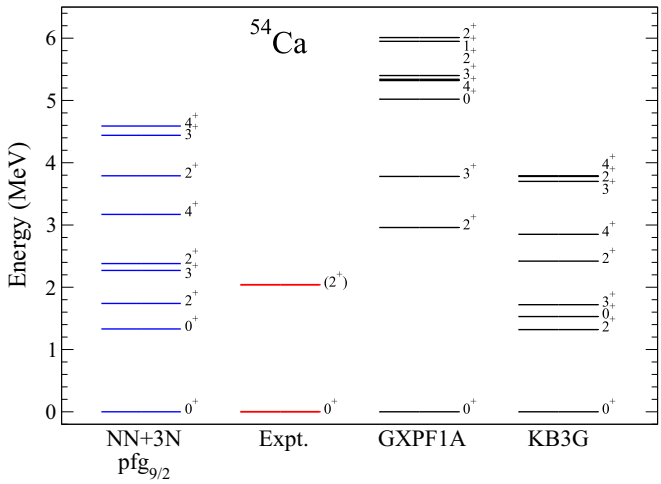

FIG. 13. (Color online) Excitation energies of bound excited states in ^{54}Ca compared with experiment [15] and phenomenological interactions (labels are as in Fig. 6).

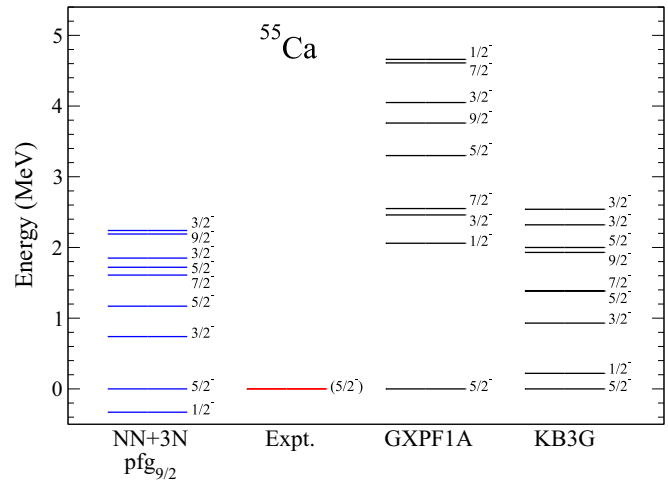

FIG. 14. (Color online) Excitation energies in ^{55}Ca compared with phenomenological interactions (labels are as in Fig. 6).

strengths of the $N = 32$ and $N = 34$ subshell closures, respectively. All three calculations predict a consistent location for the lowest $3/2^-_1$ state, also in agreement with the unassigned experimental state at 2.2 MeV which, assuming this is the correct spin assignment, reflects the predictions of the 2^+_1 state in ^{52}Ca.

Interestingly, the $5/2^-_1$ state appears at different excitation energies in all calculations: 0.8 MeV in MBPT, 1 MeV with KB3G, and 3 MeV with GXPF1A, in comparison with the state with unassigned spin at 1.75 MeV. This shows that phenomenological interactions, which give similar results close to stability, can extrapolate to very different results for neutron-rich systems. In this case, the difference is related to the small $p_{1/2}$-$f_{5/2}$ gap (weak $N = 34$ subshell closure) predicted by KB3G, and also preferred by our MBPT approach, in contrast with the large gap (strong $N = 34$ subshell closure) given by GXPF1A. Improved versions of GXPF1A that adjust the $p^2_{1/2}$ and $p_{1/2} - f_{5/2}$ $T = 1$ monopole matrix elements according to the most recent experimental data, GXPF1B and modifications, have recently become available [15,23]. They reduce the $p_{1/2}$-$f_{5/2}$ gap in agreement with experiment, and predict the $5/2^-_1$ state at 1.9 MeV. The two excited states are also in good agreement with recent CC calculations with phenomenological 3N forces, which predict the $5/2^-_1$ and $3/2^-_1$ states at 1.9 and 2.5 MeV, respectively [33].

8. ^{54}Ca

^{54}Ca is the last calcium isotope for which spectroscopic data exists. In Fig. 13, we show our NN + 3N calculations compared with the phenomenological interactions and the recent breakthrough 2^+_1 measurement at 2.043 (19) MeV [15]. Our MBPT calculations predict several low-lying excited states, implying only a weak $N = 34$ subshell closure, consistent with the spectrum in ^{53}Ca. In particular, the 2^+_1 state is predicted at 1.7 MeV [32], only 300 keV below experiment. The 2^+_1 excitation energy is also in very good agreement with 1.9 MeV predicted by CC calculations with phenomenological 3N forces [33].

The striking difference between KB3G and GXPF1A in this region is clearly manifested in ^{54}Ca. The recently measured 2^+_1 energy lies 1 MeV below GXPF1A and 0.7 MeV above the KB3G prediction. The difference between these calculations is consistent with the spectra presented in the discussion of ^{53}Ca. As in ^{53}Ca, this is improved when considering the modified GXPF1B interaction, which reproduces experiment [15].

9. ^{55}Ca and ^{56}Ca

Finally, in Figs. 14 and 15 we show NN + 3N predictions for the spectra in ^{55}Ca and ^{56}Ca. In this region the importance of the neutron $1d_{5/2}$ and $2s_{1/2}$ orbitals, currently not included in our calculations, has been emphasized in Refs. [33,63]. We plan to extend our approach to include these orbitals in the valence space and provide an improved description of very neutron-rich nuclei near $N = 40$.

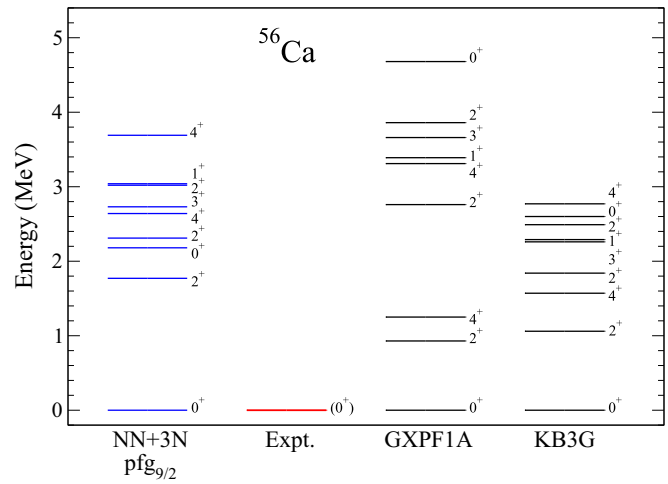

FIG. 15. (Color online) Excitation energies in ^{56}Ca compared with phenomenological interactions (labels are as in Fig. 6).

Our NN + 3N prediction for ^{55}Ca in Fig. 14 largely agrees with the predictions of the KB3G interaction, with a number of close-lying states below 2.5 MeV, in contrast to GXPF1A, where the first-excited state lies above 2 MeV. However, we find a $1/2^-$ ground state, rather than $5/2^-$ as predicted in KB3G, GXPF1A, and the CC calculations of Ref. [33]. This is consistent with the picture of a weak $N = 34$ shell closure in ^{54}Ca, where states in ^{55}Ca are not dominated by single-particle character.

In ^{56}Ca the NN + 3N 2_1^+ state is around 800 keV higher than in KB3G, GXPF1A, and CC [33], the same trend of higher 2_1^+ states than in phenomenological interactions for nonclosed even-even calcium isotopes. Otherwise, the spacing of excited states in our NN + 3N calculation is closer to KB3G. The differences between all three interactions in Fig. 15 highlight the importance of experimental spectroscopic studies beyond ^{54}Ca.

C. Electromagnetic transition strengths

1. B(E2)

Next we study electromagnetic-quadrupole ($E2$) transitions. The results of our theoretical calculations are compared with experiment [18,64] in Table II and with those of the phenomenological interactions. Standard effective charges $\delta q = 0.5e$, which take into account the reduced valence space of the calculations, are employed in all cases. Work is in progress on calculating the consistent effective one-body operators within MBPT.

Overall, we find good agreement between our valence-space calculations and experiment. The measured $B(E2)$ transitions in Table II vary widely (within a factor of 50); therefore, obtaining agreement within experimental error bars is particularly challenging. Indeed, the calculated $B(E2)$ values can deviate from experiment by up to a factor of two (or a factor of four for the small $3/2^- \to 7/2^-$ transition in ^{47}Ca), which is similar to the phenomenological interactions.

In transitions involving ^{46}Ca, the MBPT $B(E2)$ results are systematically 30% larger than with the phenomenological interactions and lie closer to experiment. Nevertheless, the predicted $2^+ \to 0^+$ transition in ^{46}Ca is still half the experimental value, pointing to important missing contributions (we also note that the two different experimental values do not overlap). In transitions involving ^{47}Ca, ^{48}Ca, and ^{49}Ca, the MBPT $B(E2)$ values are similar to those obtained with KB3G, but all calculations underestimate experiment. This also applies to GXPF1A for the $2^+ \to 0^+$ transition in ^{48}Ca. For the $3/2^- \to 7/2^-$ transition in ^{47}Ca, GXPF1A finds very good agreement with data, with the caveat that the $7/2^- \to 3/2^-$ transition in ^{49}Ca is overpredicted. The MBPT $B(E2)$ values for the $2^+ \to 0^+$ transition in ^{50}Ca are 20% larger than with the phenomenological interactions, in this case 50% higher than experiment.

TABLE II. Electric-quadrupole transition rates in the calcium isotopes compared with experiment [18,64]. The $B(E2)$ values are calculated in the $pfg_{9/2}$ space with NN + 3N interactions. Effective charges $\delta q = 0.5e$ are used in all calculations, which employ a harmonic-oscillator length $b = [\hbar/(m\omega)]^{1/2}$ with $\hbar\omega = (45A^{-1/3} - 25A^{-2/3})$ MeV and nucleon mass m. The units are e^2 fm^4.

Transition	KB3G	GXPF1A	MBPT	Expt.
^{46}Ca: $2^+ \to 0^+$	9.2	9.2	13.3	25.4 ± 4.5
				36.4 ± 2.6
^{46}Ca: $4^+ \to 2^+$	7.5	7.1	9.9	8.6 ± 2.1
^{46}Ca: $6^+ \to 4^+$	3.6	3.6	4.8	5.38 ± 0.29
^{47}Ca: $3/2^- \to 7/2^-$	0.84	3.6	1.0	4.0 ± 0.2
^{48}Ca: $2^+ \to 0^+$	11.5	11.9	10.3	19 ± 6.4
^{49}Ca: $7/2^- \to 3/2^-$	0.41	4.0	0.22	0.53 ± 0.21
^{50}Ca: $2^+ \to 0^+$	8.9	9.1	11.2	7.4 ± 0.2

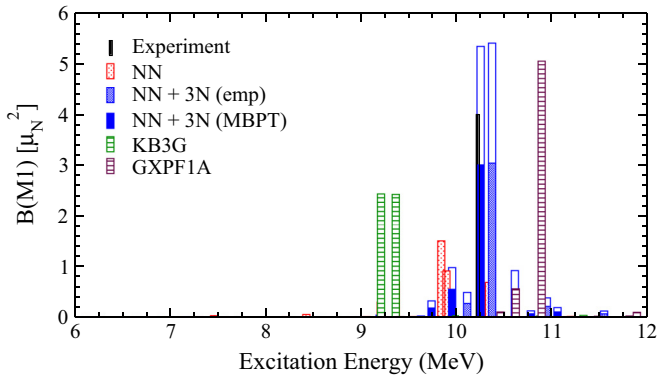

FIG. 16. (Color online) Magnetic-dipole transition rates from the ground state to 1^+ excited states in ^{48}Ca compared with experiment [67]. The $B(M1)$ values are calculated in the $pfg_{9/2}$ space with NN + 3N interactions. Spin g factors are quenched by 0.75, except for the empty blue bars.

Finally, we emphasize that electroweak two-body currents (meson-exchange currents) have not been included in our calculations of electromagnetic transitions. These were derived consistently in chiral EFT and were shown to be important for magnetic moments and electromagnetic transitions in light nuclei [65]. For axial-vector weak interactions, chiral two-body currents have been applied to medium-mass nuclei, showing that they provide important contributions to the quenching of Gamow–Teller transitions [66]. Work is in progress to extend this to electromagnetic currents and to calculate effective operators consistently in MBPT.

2. B(M1)

The magnetic-dipole ($M1$) transition between the ground state of ^{48}Ca and 1^+ excited states is compared with experiment [67] in Fig. 16. All results use spin g factors with empirical quenching $q = 0.75$, except for the empty blue bars, which give the NN + 3N results without quenching. The main conclusions of previous work using 3N forces to first order in MBPT still apply [28]. With NN forces only, the $B(M1)$ strength is strongly fragmented with a central value well below experiment. For the phenomenological interactions, GXPF1A finds a concentrated peak, while for KB3G the total strength is evenly fragmented between two peaks. We note, however, that the related KB3 interaction [68] finds no

fragmentation, which highlights the particular sensitivity of this transition to the valence-space Hamiltonian. The peaks lie about 1 MeV lower than experiment for KB3G and around 700 keV higher for GXPF1A. When 3N forces are included in the $pfg_{9/2}$ space, agreement with experimental data is clearly improved, with a concentrated peak very close to the experimental value. The effects of the improved treatment of 3N forces over that in Ref. [28] is an increase of the excitation energy of the peak transition by ∼500 keV. The degree of single-particle character of the $M1$ transition, once 3N forces are included, is similar for calculated (MBPT) or empirical (emp) SPEs. Finally, it is interesting that the NN + 3N calculations do not require a strong quenching of spin g factors. While the unquenched NN + 3N results indeed overpredict the $M1$ transition strength, they are already at the level of the quenched GXPF1A value; only a modest quenching of 0.9 would be needed to reproduce the experimental strength.

D. Residual 3N forces

We have also explored residual 3N forces, which arise between three valence nucleons in addition to their one- and two-body normal-ordered contributions. Note that, in the shell model, the normal ordering is performed with respect to the ^{40}Ca core. This does not take into account the contributions from MBPT outside of the valence space. In general, residual 3N forces are expected to lead to small corrections due to phase-space considerations for normal Fermi systems [53], because their effects are suppressed by the number of valence particles to the number of particles in the core. We have calculated the contributions from residual 3N forces at first order in perturbation theory, by using the states obtained from NN + 3N interactions at the normal-ordered one- and two-body level (as discussed in the previous sections).

In Fig. 17 we show the resulting energies $\Delta E_{\mathrm{3N,res}} = \langle\psi_n|V^{\mathrm{3N}}_{\mathrm{res}}|\psi_n\rangle$ for the ground state and first-excited state calculated in the extended $pfg_{9/2}$ space. As expected from neutron-matter calculations [69,70], residual 3N forces are repulsive. Their role is very minor for the lighter isotopes, but their contribution is amplified with neutron number, increasing to a maximum contribution of 3.7 MeV in ^{70}Ca. For the midshell $A = 55$ to 58 isotopes, only a subset of residual 3N matrix elements was used. From tests in other isotopes, we estimate the difference to using the full set to be less than 5% of the total residual 3N energy contribution.

We compare the effects of residual 3N forces with the NN + 3N ground-state energies of Fig. 4 at the normal-ordered two-body level. This shows that residual 3N forces provide small corrections to the ground-state energy, ranging from at most 3% (in ^{56}Ca) for the isotopes discussed in Sec. III B to 9% in ^{70}Ca. This justifies our perturbative estimate of residual 3N forces. As shown in Fig. 17, residual 3N contributions are similar for excited states as for ground states. Therefore, residual 3N forces lead to even smaller corrections for excitation energies, of 20 keV for ^{48}Ca, increasing to 100 keV in ^{54}Ca, and never exceeding 200 keV. As a result, the uncertainty from not including residual 3N forces is small for the results presented in the previous sections.

IV. SUMMARY

We have presented a comprehensive study of excited-state properties of calcium isotopes based on chiral NN + 3N interactions. The theoretical approach has been discussed in detail, focusing on convergence properties in the MBPT framework, benchmarking against *ab initio* CC theory for NN interactions, and exploring the role of residual 3N forces. We have presented results for ground-state energies and spectra for neutron-rich isotopes to ^{56}Ca, where 3N forces were shown to be key to understand the experimental structures. With both 3N forces and an extended $pfg_{9/2}$ valence space, we obtain a good level of agreement with experiment, where the extended space is especially important for $N \geqslant 28$. We have

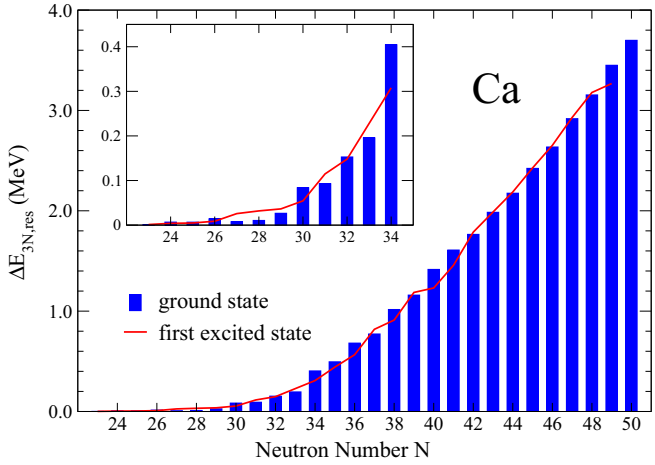

FIG. 17. (Color online) First-order contribution from residual 3N forces to the energies of the ground state (bars) and first-excited state (solid line) of the calcium isotopes in the extended $pfg_{9/2}$ valence space.

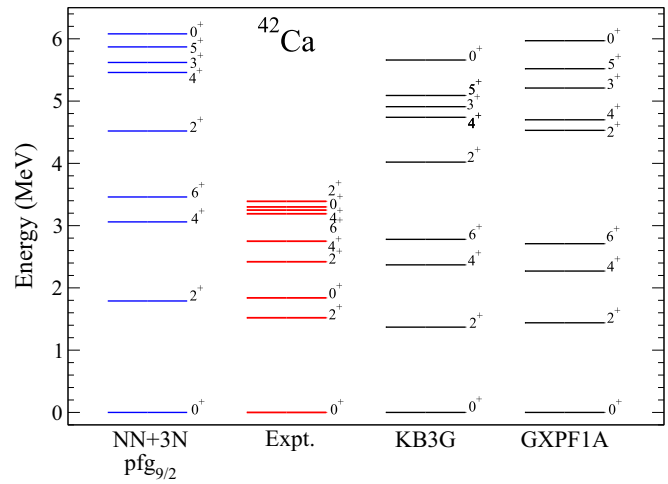

FIG. 18. (Color online) Excitation energies of bound excited states in ^{42}Ca compared with experiment and phenomenological interactions (labels are as in Fig. 6).

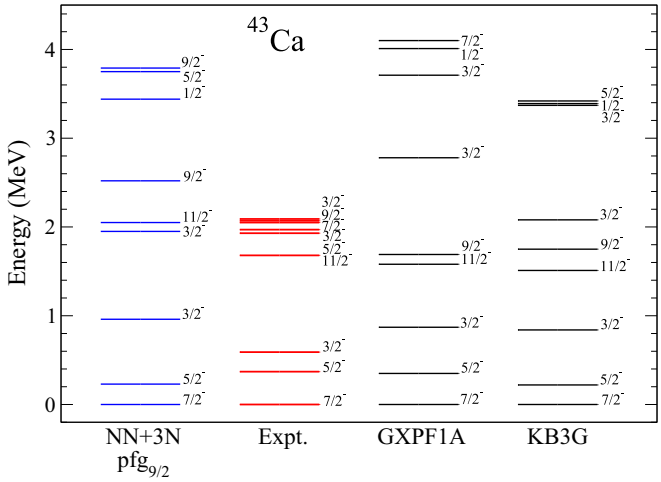

FIG. 19. (Color online) Excitation energies of bound excited states in ^{43}Ca compared with experiment and phenomenological interactions (labels are as in Fig. 6).

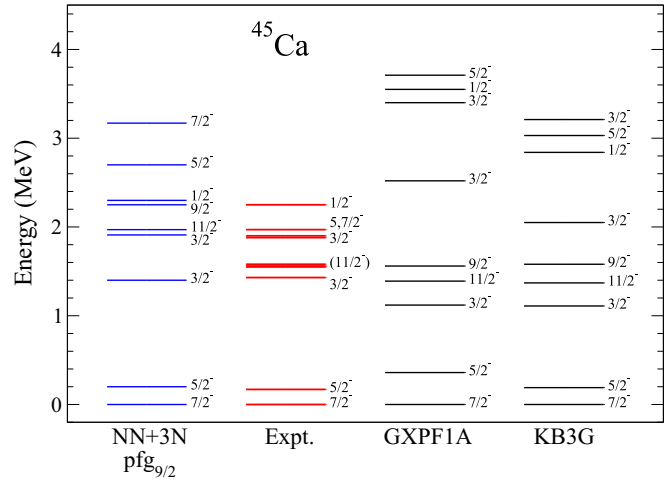

FIG. 21. (Color online) Excitation energies of bound excited states in ^{45}Ca compared with experiment and phenomenological interactions (labels are as in Fig. 6).

also studied electromagnetic $E2$ and $M1$ transitions, finding that experimental data are well described by our calculations. Where data does not exist, our results provide predictions for unexplored properties of neutron-rich calcium isotopes.

Future work will include studies of the theoretical uncertainties due to the input Hamiltonian and the RG or SRG evolution. In addition, the recent development of the IMSRG for open-shell [71,72] and CC calculations of effective interactions [73] enable nonperturbative derivations of valence-space Hamiltonians, which will also provide benchmarks for MBPT calculations.

ACKNOWLEDGMENTS

We thank G. Hagen for helpful discussions. This work was supported by the BMBF Contract No. 06DA70471, the DFG through Grant No. SFB 634, the ERC Grant No. 307986 STRONGINT, and the Helmholtz Alliance HA216/EMMI. Computations were performed on JUROPA at the Jülich Supercomputing Center and on Kraken at the National Institute for Computational Sciences.

APPENDIX: SPECTRA OF LIGHT CALCIUM ISOTOPES $A < 47$

We present the spectra for the lighter $^{42–46}$Ca in Figs. 18–22. Our results are in good agreement with experiment [62] and generally exhibit quality comparable to phenomenological interactions. The only exceptions are the 4^+,6^+ states in ^{46}Ca, $\sim$1 MeV higher than in experiment, in contrast to phenomenology. Note that some excited states, like the 0_2^+ states in ^{42,44,46}Ca, are expected to be dominated by sd-shell degrees of freedom, and are therefore not present in our theoretical results.

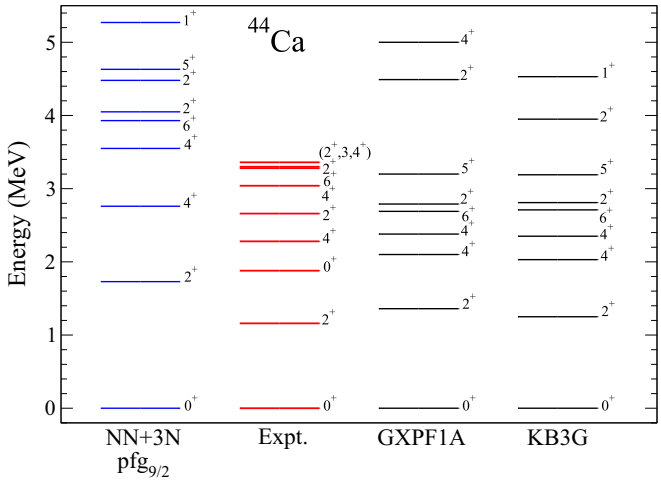

FIG. 20. (Color online) Excitation energies of bound excited states in ^{44}Ca compared with experiment and phenomenological interactions (labels are as in Fig. 6).

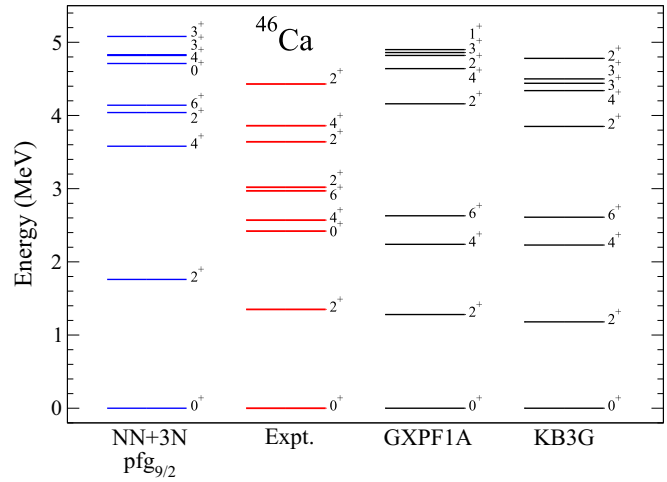

FIG. 22. (Color online) Excitation energies of bound excited states in ^{46}Ca compared with experiment and phenomenological interactions (labels are as in Fig. 6).

[1] T. Baumann, A. Spyrou, and M. Thoennessen, Rep. Prog. Phys. **75**, 036301 (2012).
[2] O. Sorlin and M.-G. Porquet, Prog. Part. Nucl. Phys. **61**, 602 (2008).
[3] A. Huck, G. Klotz, A. Knipper, C. Miehé, C. Richard-Serre, G. Walter, A. Poves, H. L. Ravn, and G. Marguier, Phys. Rev. C **31**, 2226 (1985).
[4] A. Gade, R. V. F. Janssens, D. Bazin, R. Broda, B. A. Brown, C. M. Campbell, M. P. Carpenter, J. M. Cook, A. N. Deacon, D. C. Dinca *et al.*, Phys. Rev. C **74**, 021302(R) (2006).
[5] R. V. F. Janssens, B. Fornal, P. F. Mantica, B. A. Brown, R. Broda, P. Bhattacharyya, M. P. Carpenter, M. Cinausero, P. J. Daly, A. D. Davies *et al.*, Phys. Lett. B **546**, 55 (2002).
[6] P. F. Mantica, R. Broda, H. L. Crawford, A. Damaske, B. Fornal, A. A. Hecht, C. Hoffman, M. Horoi, N. Hoteling, R. V. F. Janssens *et al.*, Phys. Rev. C **77**, 014313 (2008).
[7] H. L. Crawford, R. V. F. Janssens, P. F. Mantica, J. S. Berryman, R. Broda, M. P. Carpenter, N. Cieplicka, B. Fornal, G. F. Grinyer, N. Hoteling *et al.*, Phys. Rev. C **82**, 014311 (2010).
[8] J. I. Prisciandaro, P. F. Mantica, B. A. Brown, D. W. Anthony, M. W. Cooper, A. Garcia, D. E. Groh, A. Komives, W. Kumarasiri, P. A. Lofy *et al.*, Phys. Lett. B **510**, 17 (2001).
[9] A. T. Gallant, J. C. Bale, T. Brunner, U. Chowdhury, S. Ettenauer, A. Lennarz, D. Robertson, V. V. Simon, A. Chaudhuri, J. D. Holt *et al.*, Phys. Rev. Lett. **109**, 032506 (2012).
[10] F. Wienholtz, D. Beck, K. Blaum, Ch. Borgmann, M. Breitenfeldt, R. B. Cakirli, S. George, F. Herfurth, J. D. Holt, M. Kowalska *et al.*, Nature (London) **498**, 346 (2013).
[11] N. Marginean, S. M. Lenzi, A. Gadea, E. Farnea, S. J. Freeman, D. R. Napoli, D. Bazzacco, S. Beghini, B. R. Behera, P. G. Bizzeti *et al.*, Phys. Lett. B **633**, 696 (2006).
[12] S. N. Liddick, P. F. Mantica, R. V. F. Janssens, R. Broda, B. A. Brown, M. P. Carpenter, B. Fornal, M. Honma, T. Mizusaki, A. C. Morton *et al.*, Phys. Rev. Lett. **92**, 072502 (2004).
[13] D.-C. Dinca, R. V. F. Janssens, A. Gade, D. Bazin, R. Broda, B. A. Brown, C. M. Campbell, M. P. Carpenter, P. Chowdhury, J. M. Cook *et al.*, Phys. Rev. C **71**, 041302 (2005).
[14] M. Rejmund, S. Bhattacharyya, A. Navin, W. Mittig, L. Gaudefroy, M. Gelin, G. Mukherjee, F. Rejmund, P. Roussel-Chomaz, and Ch. Theisen, Phys. Rev. C **76**, 021304(R) (2007).
[15] D. Steppenbeck, S. Takeuchi, N. Aoi, P. Doornenbal, M. Matsushita, H. Wang, H. Baba, N. Fukuda, S. Go, M. Honma *et al.*, Nature (London) **502**, 207 (2013).
[16] F. Perrot, F. Maréchal, C. Jollet, Ph. Dessagne, J. C. Angélique, G. Ban, P. Baumann, F. Benrachi, U. Bergmann, C. Borcea *et al.*, Phys. Rev. C **74**, 014313 (2006).
[17] B. Fornal, R. V. F. Janssens, R. Broda, N. Marginean, S. Beghini, L. Corradi, M. P. Carpenter, G. De Angelis, F. Della Vedova, E. Farnea *et al.*, Phys. Rev. C **77**, 014304 (2008).
[18] D. Montanari, S. Leoni, D. Mengoni, J. J. Valiente-Dobon, G. Benzoni, N. Blasi, G. Bocchi, P. F. Bortignon, S. Bottoni, A. Bracco *et al.*, Phys. Rev. C **85**, 044301 (2012).
[19] E. Caurier, G. Martinez-Pinedo, F. Nowacki, A. Poves, and A. P. Zuker, Rev. Mod. Phys. **77**, 427 (2005).
[20] A. Poves, J. Sánchez-Solano, E. Caurier, and F. Nowacki, Nucl. Phys. A **694**, 157 (2001).
[21] M. T. Honma, T. Otsuka, B. A. Brown, and T. Mizusaki, Phys. Rev. C **69**, 034335 (2004).
[22] M. T. Honma, T. Otsuka, B. A. Brown, and T. Mizusaki, Eur. Phys. J. A **25**, 499 (2005).
[23] Y. Utsuno, T. Otsuka, B. A. Brown, M. T. Honma, T. Mizusaki, and N. Shimizu, Phys. Rev. C **86**, 051301(R) (2012).
[24] T. R. Rodriguez and J. L. Egido, Phys. Rev. Lett. **99**, 062501 (2007).
[25] M. Hjorth-Jensen, T. T. S. Kuo, and E. Osnes, Phys. Rep. **261**, 125 (1995).
[26] A. P. Zuker, Phys. Rev. Lett. **90**, 042502 (2003).
[27] H.-W. Hammer, A. Nogga, and A. Schwenk, Rev. Mod. Phys. **85**, 197 (2013).
[28] J. D. Holt, T. Otsuka, A. Schwenk, and T. Suzuki, J. Phys. G **39**, 085111 (2012).
[29] T. Otsuka, T. Suzuki, J. D. Holt, A. Schwenk, and Y. Akaishi, Phys. Rev. Lett. **105**, 032501 (2010).
[30] J. D. Holt, J. Menéndez, and A. Schwenk, Eur. Phys. J. A **49**, 39 (2013).
[31] J. D. Holt, J. Menéndez, and A. Schwenk, Phys. Rev. Lett. **110**, 022502 (2013).
[32] J. D. Holt, J. Menéndez, and A. Schwenk, J. Phys. G **40**, 075105 (2013).
[33] G. Hagen, M. Hjorth-Jensen, G. R. Jansen, R. Machleidt, and T. Papenbrock, Phys. Rev. Lett. **109**, 032502 (2012).
[34] V. Somà, C. Barbieri, and T. Duguet, Phys. Rev. C **87**, 011303 (2013).
[35] V. Somà, A. Cipollone, C. Barbieri, P. Navrátil, and T. Duguet, Phys. Rev. C **89**, 061301(R) (2014).
[36] R. Roth, S. Binder, K. Vobig, A. Calci, J. Langhammer, and P. Navrátil, Phys. Rev. Lett. **109**, 052501 (2012).
[37] K. Tsukiyama, S. K. Bogner, and A. Schwenk, Phys. Rev. Lett. **106**, 222502 (2011).
[38] H. Hergert, S. K. Bogner, S. Binder, A. Calci, J. Langhammer, R. Roth, and A. Schwenk, Phys. Rev. C **87**, 034307 (2013).
[39] E. Epelbaum, H.-W. Hammer, and U.-G. Meißner, Rev. Mod. Phys. **81**, 1773 (2009).
[40] R. Machleidt and D. Entem, Phys. Rep. **503**, 1 (2011).
[41] C. Caesar, J. Simonis, T. Adachi, Y. Aksyutina, J. Alcantara, S. Altstadt, H. Alvarez-Pol, N. Ashwood, T. Aumann, V. Avdeichikov *et al.*, Phys. Rev. C **88**, 034313 (2013).
[42] G. Hagen, T. Papenbrock, M. Hjorth-Jensen, and D. J. Dean, arXiv:1312.7872.
[43] T. T. S. Kuo and E. Osnes, Lect. Notes Phys. **364**, 1 (1990).
[44] S. K. Bogner, T. T. S. Kuo, L. Coraggio, A. Covello, and N. Itaco, Phys. Rev. C **65**, 051301(R) (2002).
[45] L. Coraggio, A. Covello, A. Gargano, and N. Itaco, Phys. Rev. C **80**, 044311 (2009).
[46] S. K. Bogner, T. T. S. Kuo, and A. Schwenk, Phys. Rep. **386**, 1 (2003).
[47] S. K. Bogner, R. J. Furnstahl, and A. Schwenk, Prog. Part. Nucl. Phys. **65**, 94 (2010).
[48] D. R. Entem and R. Machleidt, Phys. Rev. C **68**, 041001(R) (2003).
[49] S. K. Bogner, R. J. Furnstahl, S. Ramanan, and A. Schwenk, Nucl. Phys. A **784**, 79 (2007).
[50] U. van Kolck, Phys. Rev. C **49**, 2932 (1994).
[51] E. Epelbaum, A. Nogga, W. Glöckle, H. Kamada, Ulf.-G. Meißner, and H. Witała, Phys. Rev. C **66**, 064001 (2002).
[52] S. K. Bogner, R. J. Furnstahl, A. Nogga, and A. Schwenk, arXiv:0903.3366; K. Hebeler, S. K. Bogner, R. J. Furnstahl, A. Nogga, and A. Schwenk, Phys. Rev. C **83**, 031301(R) (2011).
[53] B. Friman and A. Schwenk, in *From Nuclei to Stars: Festschrift in Honor of Gerald E. Brown*, edited by S. Lee (World Scientific, Singapore, 2011), p. 141.

[54] G. Hagen, T. Papenbrock, D. J. Dean, A. Schwenk, A. Nogga, M. Wloch, and P. Piecuch, Phys. Rev. C **76**, 034302 (2007).
[55] G. Hagen, T. Papenbrock, D. J. Dean, and M. Hjorth-Jensen, Phys. Rev. C **82**, 034330 (2010).
[56] E. Caurier and F. Nowacki, Acta Phys. Pol. B **30**, 705 (1999).
[57] D. J. Dean, M. T. Ressell, M. Hjorth-Jensen, S. E. Koonin, K. Langanke, and A. P. Zuker, Phys. Rev. C **59**, 2474 (1999).
[58] E. Caurier, J. Menéndez, F. Nowacki, and A. Poves, Phys. Rev. C **75**, 054317 (2007).
[59] G. Audi, M. Wang, A. H. Wapstra, F. G. Kondev, M. MacCormick, X. Xu, and B. Pfeiffer, Chin. Phys. C **36**, 1287 (2012).
[60] S. Okubo, Prog. Theor. Phys. **12**, 603 (1954).
[61] S. Y. Lee and K. Suzuki, Phys. Lett. B **91**, 173 (1980).
[62] http://www.nndc.bnl.gov/ensdf/.
[63] S. M. Lenzi, F. Nowacki, A. Poves, and K. Sieja, Phys. Rev. C **82**, 054301 (2010).
[64] S. Raman, C. W. G. Nestor Jr., and P. Tikkanen, At. Data Nucl. Data Tables **78**, 1 (2001).
[65] S. Pastore, S. C. Pieper, R. Schiavilla, and R. B. Wiringa, Phys. Rev. C **87**, 035503 (2013).
[66] J. Menéndez, D. Gazit, and A. Schwenk, Phys. Rev. Lett. **107**, 062501 (2011).
[67] P. von Neumann-Cosel, A. Poves, J. Retamosa, and A. Richter, Phys. Lett. B **443**, 1 (1998).
[68] A. Poves and A. Zuker, Phys. Rep. **70**, 235 (1981).
[69] K. Hebeler and A. Schwenk, Phys. Rev. C **82**, 014314 (2010).
[70] K. Hebeler and A. Schwenk, Eur. Phys. J. A **50**, 11 (2014).
[71] K. Tsukiyama, S. K. Bogner, and A. Schwenk, Phys. Rev. C **85**, 061304(R) (2012).
[72] S. K. Bogner, H. Hergert, J. D. Holt, A. Schwenk, S. Binder, A. Calci, J. Langhammer, and R. Roth, arXiv:1402.1407.
[73] G. R. Jansen, J. Engel, G. Hagen, P. Navrátil, and A. Signoracci, arXiv:1402.2563.